Soft Matter

PAPER

View Article Online
View Journal | View Issue

Cite this: *Soft Matter*, 2022, **18**, 8262

Elastogranular columns and beams

Arman Guerra, †[a] Casey Lautzenhiser, †[a] Xin Jiang, [a] Kate Flanagan,[a] David Rak,[a] Skylar Tibbits[b] and Douglas P. Holmes*[a]

Received 27th July 2022,
Accepted 10th October 2022

DOI: 10.1039/d2sm01010k

rsc.li/soft-matter-journal

String and grains can be combined to create structures capable of bearing significant loads. In this work, we prepare columns and beams through a layer-by-layer deposition of granular matter and loops of fiber strings, and characterize their mechanical properties. The loops cause the grains to jam, and the inter-grain contact leads to a Hertzian-like constitutive response. Initially, one force chain that propagates vertically through the column bears most of the compressive load. As the magnitude of the load is increased, more force chains form in the column, which act in parallel to increase its stiffness, akin to a "super-Hertzian" regime. Applying a compressive prestress enables the structures to withstand shear, enabling the fabrication of cantilevered beams. This work provides a mechanical framework to use elastogranular jamming to create rapid, reusable infrastructure components, such as columns, beams, and arches from inexpensive, commonplace materials, such as rocks and string.

1 Introduction

The art of dry stone walling is considered by UNESCO to be one of the intangible cultural heritages of humanity.[1] Dry stone structures lack mortar, and rely on the precise, layer-by-layer placement of stones to provide structural integrity. In lieu of an adhesive binder, the combination of friction and geometric interlocking provides the structures with significant strength, a process more generally described by the jamming of granular matter. Granular matter will jam, undergoing a phase transition from a fluid-like state to a solid-like state, when the density of the granular packing reaches a critical point.[2–5] As this density of particles increases, so does the number of contacts that a particular grain has with its neighbors, until the packing is said to be jammed and isostatic, and each particle is in a state of mechanical equilibrium. The jammed state is strongly dependent on several criteria, including the frictional properties, shape, and polydispersity of the grains, and it has been shown that truly novel and complex physics develop near the jamming point.[6] Once the system reaches the jammed state, the collective behavior of the grains is akin to a solid material. However, for packings of disordered particles at low pressure near this jamming transition, global forcing does not trivially translate to local contacts, and these systems show increasingly complex deformation fields under shear loading.[7] As a result, while the total granular structure can withstand large applied loads in some directions, they may be quite fragile when loaded in others.[8] This interplay is why grains can sustain a finite angle of repose under the influence of gravity,[9] and yet require intricate placement with interlocking shapes to adopt more complex forms.[10–13]

The stabilization of soils is perhaps even more tightly entwined with human history than the art of dry stone walling. Chemical stabilization, by the addition of lime to soils, was used by early civilizations in Mesopotamia and Egypt.[14,15] For thousands of years, humans have lived in dwellings made of bricks formed by combining mud and straw.[16] The underlying principles of chemically or structurally reinforcing earth were revisited in the late 1960's,[17] with a particular focus on stabilizing slopes prone to erosion.[18] Soil erosion is often caused by deforestation and the displacement of deep-rooted grasses, as networks of plant roots act as stabilizers.[19–21] In addition to these natural stabilizers, there has been a sustained interest in using synthetic fibers as a means to stabilize a variety of subterranean granular matter, including soils,[22–25] sand,[26–29] aggregates,[30,31] silt,[32] and ash[33] stabilized by synthetic fibers, yarns, geotextiles, laminates, and randomly oriented inclusions.

The addition of elastic fibers with a negligible bending rigidity to a granular medium increases the number of contacts on each grain, and adding additional confinement to the granular particles. It has been shown that highly confined granular materials behave qualitatively different from loose or bulk grains.[34–36] In this case, the added confinement allows jamming to occur at a lower granular packing density. In turn, the entangled network of fibers gives the grains an intermediate, scale reinforcing structure. Granular jamming caused by the confinement of a slender body inside a granular medium results in an intricate coupling of elastic and granular

[a] *Mechanical Engineering, Boston University, Boston, MA, 02215, USA. E-mail: dpholmes@bu.edu*
[b] *MIT, Massachusetts Avenue 77, Cambridge, MA 02139, USA*
† These authors contributed equally to this work.

interactions that exhibit bending, buckling, and reconfiguration of the slender elastic structure and its surrounding grains.[37–41] Tuning particle shape alone has a strong influence on the mechanical response of granular materials.[11,42,43] Combining elastic and granular materials to form an elastogranular structure[38] can allow for further reinforcement, and enable the formation of jammed, free-standing elastogranular architecture.[44–46] Engineering elastogranular columns and barriers presents a means for large-scale, reversible and reusable structures,[10,12,47] which present modern analogs to subterranean elastogranular reinforcement, a task previously achieved using mechanically stabilized earth[48] and fabric.[49] Current research efforts in architectural jamming[10,12,47] have demonstrated that elastogranular structures can be utilized as engineering structures if we can better understand how to design and build them with designed mechanical properties.

While the mechanics of subterranean elastogranular structures have been examined using triaxial testing and numerical methods,[50–52] much less is understood about free-standing structures. The authors recently examined the minimum criteria to enable free-standing elastogranular structures, finding that for columns of grains surrounded by loops of fiber, the critical spacing $S_c/2R = \max\left(3\sin\alpha, \frac{2\sin\alpha+1}{1+2\beta_{he}}\right)$ of exterior loops is a function of the grain radius (R), the angle of repose (a proxy measure of friction and grain geometry, α), and a dimensionless, hydroelastic scale β_{he} which is a ratio between the hydrostatic force from the grains on the loops and their bending rigidity.[53] When the weight of the grains is large compared to their bending rigidity, *i.e.* when β_{he} is large, friction dominates and the angle of repose sets the critical minimum spacing to form a free-standing column. Rigid loops, *i.e.* when β_{he} is small, can increase this minimum spacing when the hydrostatic load is small. While this initial work determined the criteria to form structures that can bear their own weight, it did not provide insight into their mechanical response to external loads.

In this work, we examine the mechanical response of elastogranular columns and beams prepared with a variety of granular matter and fiber reinforcement (Fig. 1). We find that the stiffness of the columns is a function of the grain stiffness, average radii, and degree of order of the granular material, while the stability of grains within the column, and therefore the "smoothness" of their loading response, depends on the amount of added fiber. Finally, we will examine the effects of shear on columns by compressing them and then orienting them horizontally like cantilever beams. With sufficient preload, elastogranular beams can bear significant load perpendicular to their long axis, providing a resistance to shear that is proportional to the magnitude of the applied compressive load.

Fig. 1 (a) Elastogranular columns increasing in scale with a fixed volumetric ratio of fibers to grains. Jamming facilitates the formation of elastogranular (a) columns, (b) cantilever beams, and (c) arches. All scale bars 40 mm.

2 Columns

2.1 Experiments

For this work, we prepared elastogranular columns *via* the layer-by-layer deposition of rocks and loops of fiber within a slip-cast mold. We used a variety of particles to represent a range of frictional properties, and stiffness, including crushed marble, granite, sandstone, rubber spheres, plastic garden stones, and chopped rubber particles (average grain radii R ranging from 1–1.25 cm). We studied elastogranular columns prepared with two types of elastic fiber loops: exterior loops of radius 40 mm, and interior loops of radius 15 mm (twisted nylon, 18 gauge). Slip-cast molds were prepared with a piece of Mylar film (0.127 mm thick, McMaster) taped into a cylinder of the target diameter (80 mm) and height (120 mm). To form a layer we deposited grains by hand, and tamped gently with a circular acrylic plunger until we reached a desired layer thickness approximately equal to the average grain diameter $2R$. During this deposition process, we placed exterior fiber loops at consistent intervals such that the loops were evenly spaced, and no loops overlapped as depicted in Fig. 2. For columns prepared with both interior and exterior fiber, we also placed multiple internal loops as depicted in Fig. 2. To parameterize the amount of external and internal fiber, we consider the area ratio $\psi_e = A_e/A_C$ and volume ratio $\psi_i = V_i/V_L$ respectively, where V_i is the total volume of interior fiber in one layer, V_L is the volume of rock in one layer, A_e is the total surface area of external fiber coverage, and A_C is the total surface area of the column. Note that minimum A_e is controlled by the critical loop spacing.[53] To understand what effect the fiber has on the mechanical properties of the columns, we constructed many columns, varying ψ_e from 0.13 to 0.76 at $\psi_i = 0$, and ψ_i from 0 to 0.05 at $\psi_e = 0.26$.

We then removed the mold and probed their mechanical properties. We performed displacement-controlled compression tests using an Instron 5943 (maximum load 500 N) at a rate of 5 mm min^{-1}. Excluding the cyclical loading described in Fig. 3, ten compression tests were run for each sample: the first to a maximum load of 450 N, the subsequent cyclical tests

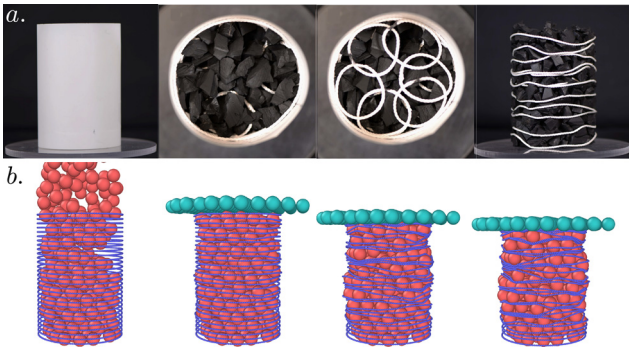

Fig. 2 (a) The process for column construction utilizing both interior and exterior fibers. From left to right – the empty cylindrical mold – the top–down view of the method of construction within the cylindrical mold – a completed column. (b) Simulation images of a column being constructed and subsequently loaded.

(loading/unloading) to a maximum load of 200 N. For the entirety of this loading process, we also measure the displacement of the loading plate (which is equivalent to the end-shortening in the columns) δ. In this work we only analyze experimental data in this force range because of the limitations of our equipment. However, we have also seen that these columns can handle a much larger load than we could probe – for instance, when compressed in a hydraulic press, columns constructed with marble grains could withstand a load capacity of 30 kN, and only collapsed when the grains began to pulverize.

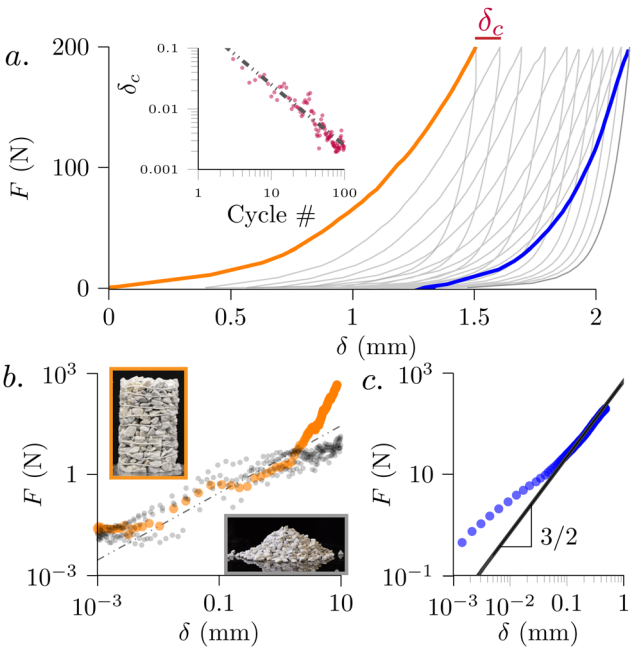

Fig. 3 (a) The first 11 cycles of the loading of a cylinder. In the inset we show how δ_c decreases with cycle number. (inset) The plastic deformation of a column seems to scale with the inverse of the cycle number. (b) We zoom in on the first (orange) loading cycle of the column, and compare it with five loadings of piles of grains. The dotted line is an empirical fit with a slope of 1. (c) The loading response (blue line taken from (a) above) eventually adopts a slope of 3/2 corresponding to a Hertzian response.

2.2 Numerical simulations

In addition to our physical experiments, we also performed numerical simulations to allow for precision in fiber placement and for construction of columns with extreme values of ψ_e (values near S_c and values near the saturation limit, where $A_e \approx A_c$). These simulations also allowed us to investigate the processes internal to the columns, motivating the analysis that we used to understand the nature of their mechanical response. We implement numerical simulations using the Large-scale Atomic/Molecular Massively Parallel Simulator (LAMMPS)[54] in the manner outlined in Guerra (2021)[53] (Fig. 2). The simulated columns had the same dimensions as the physical columns, a grain diameter of 1.1 cm, and fiber diameter 1.5 mm. For the grains, we consider spherical particles with similar characteristics to hard rubber (Young's modulus $E_g = 6.5 \times 10^7$ Pa, Poisson's ratio $\nu = 0.4$, coefficient of sliding friction $\mu_s = 1.16$ and rolling friction $\mu_r = 1$), and for the fibers we consider loops with Young's modulus $E_s = 10^9$ Pa. We vary ψ_e from 0.38 to 0.89, and use $\psi_i = 0$, that is, we do not consider any simulations with internal fiber, simply because simulating fiber is computationally expensive. We also do not perform any simulations of the cantilever beams for the same reason. We discuss these and other possible additional simulations in the conclusions.

For each simulation, grains are randomly poured into a cylinder while the fibers are fixed in place. That cylinder is then removed, the fibers freed, and a circular force plate is inserted on top of the column (Fig. 2). Due to the computational demand of the simulations, loading rate could not be matched to physical experiments, however we found that a loading rate of 100 N s^{-1} was sufficiently slow to ensure an iso-static response. The compression cycles were modeled after physical experiments and begin with a strain surface setting cycle with a peak load of 450 N, followed by 3 subsequent cycles with peak loads of 200 N. All image analyses and visualizations of simulated columns are completed using the Open Visualization Tool (OVITO).[55] We found that the simulations displayed similar qualitative and quantitative (Fig. 4) characteristics to physical experiments throughout the loading process.

2.3 Analysis

The primary means by which we will characterize the mechanical properties of these elastogranular systems is through the use of force–displacement analyses, in which load is applied to an object, and the displacement is measured at the point of contact with the loading apparatus. In Fig. 3, we show the first 11 cycles of the force–displacement response of a column cyclically loaded in uniaxial compression $N = 100$ times, where each cycle has a peak load of 200 N. There is a significant amount of hysteresis between loading and unloading the column, especially at small N, and some of this dissipation occurs due to the plastic-like permanent deformation of the column due to a cycle of loading, which we refer to as δ_c. We find that $\delta_c/H \sim N^{-1}$ (Fig. 3a inset). If we zoom in on the first cycle (Fig. 3b), we see the source of this plastic deformation – for small displacements the force response appears to be

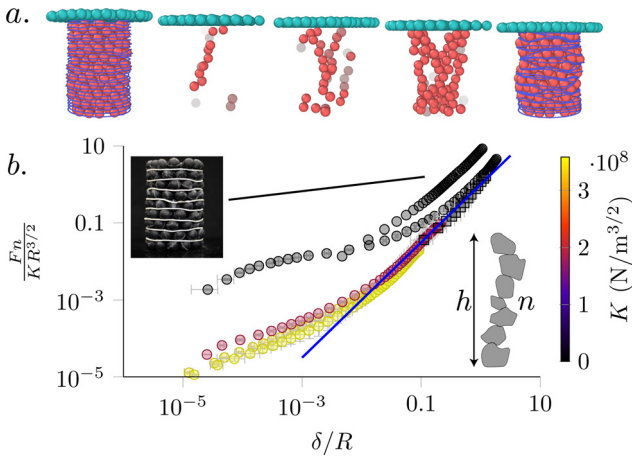

Fig. 4 (a) Simulation images where the load on the column is increasing from left to right. In the center three images, the opacity of the granular particles is set by the pressure from other particles, the loading cell, and the floor (note that less opaque grains may appear gray). We see that the number of force chains increases with load, starting with just one chain. (b) If we nondimensionalize F and δ using eqn (3) – that is, if we assume that the stiffness of a column is the stiffness of one continuous force chain – we find that the force–displacement curves (experiments – circles, simulations – squares) of all column types (after the initial grain-settling period at low δ) fall onto the directly predicted curve (blue line), with the exception of the rubber spheres, which pack into a lattice, increasing the stiffness of those columns. The data is colored by the Hertzian stiffness K.

similar to that of a pile of grains loaded in compression under small displacement, where the majority of that displacement is due to rearrangement of particles. We find empirically that this seems to follow a power law of $F \sim \delta$, although we do not propose a mechanism for why that is the case. The experimental setup described in this work (and our capacity for visualizing granular of the grains) is not sensitive enough to capture these small rearrangements at low δ, and the simulation time to develop a framework for this behavior is prohibitive, and therefore we leave a more mechanistic approach to the low-displacement force response of elastogranular structures to future work.

In Fig. 3c, we show the force–displacement curve for one of the later loading cycles from Fig. 3a. We find that, after this initial grain rearrangement regime, in this log–log plot the curve approaches a slope of $\approx 3/2$. We can understand this behavior through classical approaches for analyzing the contact between two non-adhesive elastic spherical bodies, as developed by Hertz (1882)[56] and further extended by Johnson (1987).[57] This approach yields the following relation between force (F) and displacement (δ)

$$F = K\delta^{3/2}. \tag{1}$$

where $K = (4/3)E^*R^{*1/2}$ is the "Hertzian stiffness," $E^* = ((1-\nu_1^2)/E_1 + (1-\nu_2^2)/E_2)^{-1}$ is the effective Young's modulus, $R^* = R_1R_2/(R_1+R_2)$ is the effective radius, and E_i, ν_i, and R_i are the Young's moduli, Poisson's ratios, and radii of the bodies. We might expect then that this 3/2 slope in the force–displacement is due to the elastic deformation of the granular materials, since any elastic deformation of the fiber would induce a different slope.[58]

Next, we will build upon the contact mechanics of single particle response to understand the response of the elastogranular columns. In Fig. 4a, we show simulations of a specific column at increasing load from left to right, where the opacity of the granular particles is set by their pressure. We can see that at low load, there is approximately a single "force chain"[59–62] which traverses from the top of the column to the bottom. As this load increases and the particles deform, the number of force chains increases until many grains are part of a force chain. We can predict the force–displacement response of a force chain (assuming all particles remain in contact over the course of their loading, and particles do not slide against eachother) by considering the particles as being in-series with eachother, such that their total stiffness will be

$$\frac{1}{K_c} = \sum_{I=1}^{n} \frac{1}{K_i} \tag{2}$$

where K_c is the stiffness of the chain of grains, n is the number of grains in a chain, and K_i is the stiffness of grain i. This simply comes from the fact that if you compress a stack of particles (such as the one shown in the inset of Fig. 4b) each particle experiences the same compressive force, and so the total deformation is simply the sum of the deformations of each particle. Since the stiffness is inversely proportional to the deformation, it is also inversely proportional to the number of particles. Instead of using the mathematical value of K listed above (since we do not know the Young's moduli of our particles, or the average radii R_i of the surface features of the grains), we perform additional force–displacement experiments on single grains, and find an average fit value of K for each particle type. If we assume that the stiffness of each grain is the same, then we have that $K_c = K/n$. If we consider only one force chain to be bearing the majority of the load (Fig. 4a) then we would expect that the stiffness of the entire column would simply be the stiffness of one force chain. Or in other words, combining eqn (1) with the predicted chain stiffness (K/n) and rearranging,

$$\frac{Fn}{KR^{3/2}} = \left(\frac{\delta}{R}\right)^{3/2} \tag{3}$$

In Fig. 4b we plot this non-dimensionalized response – where the data is colored by our fit values of K – for all grain types (circles), and for our simulated columns (squares). All force–displacement curves indeed collapse to what eqn (3) indicates, except for the experiments with rubber spheres. During construction of columns with these particles, because of the careful layer-by layer approach, these particles tended to pack into a regular lattice. We expect that, because of this lattice arrangement, multiple force chains become active closer to the beginning of the loading cycle (though not all of them, as force networks are still disordered in lattice arrangements of granular particles[63]). We expect that it is this effect that leads the columns to be stiffer than our model predicts.

For much of the post-grain-settling (elastic) section of the force–displacement response of these columns, we indeed find that the response fits well into the classical 3/2 understanding of grain contact. And indeed, for some grain types, especially those with higher K, the responses match this classical prediction for the entire loading cycle. However, we find that when δ reaches the order of a grain radius (which we only observed for some grain types, as we were not able to compress columns made with very stiff grains this much Fig. 4b), the columns seem to adopt a new response. We zoom in on the high-δ section of the force–displacement curves of the rubber chunks in Fig. 5c, and find that at a consistent value of δ/R, the columns transition into a "super-Hertzian" regime, where the force becomes proportional to a higher-than-3/2 exponent of δ.

We already know, however, that when the force on the columns is significant, the number of force-chains which are in compression increases. This is analogous to the Steuermann extension of Hertzian contact,[57,64] in that the columns begin to "conform" to the applied load. When only one force chain is loaded (at low δ), the stiffness of the column is simply the stiffness of this chain. But, as the displacement increases and more force chains become loaded (Fig. 5a), they bear the load in parallel, and we would expect that the in-parallel stiffness of multiple chains is larger than the stiffness of one single chain. We can formulate this mathematically based on the illustration in Fig. 5b. We consider a column to be made up of m force chains which will become activated at different δ. We call δ_j the necessary column displacement such that force chain j will become active. If this arrangement is loaded, we would expect that

$$\frac{Fn}{KR^{3/2}} = \sum_{i=1}^{m} \mathrm{Heav}(\delta - \delta_i)\left(\frac{\delta - \delta_i}{R}\right)^{3/2} \tag{4}$$

where the Heaviside step function (Heav(x) = 1 if $x > 0$, 0 otherwise) simply ensures that we do not count any force chains which are not yet loaded. In more plain terms, this equation models the idea that force chain i will only become active once we have surpassed the necessary displacement δ_i such that it activates. Furthermore, once it is active, it will respond to its loading with a force given by eqn (1) where the displacement is offset by δ_i. We can also define $\gamma_j = \delta_{j+1} - \delta_j$ to be the displacement between the formation of force chains j and $j + 1$. In other words, once we have activated force chain j, we must compress the column an additional γ_j to activate force chain $j + 1$. If we assume that the height difference between subsequent force chains is on the order of one grain radius $\gamma_i = \gamma = r$, we can find a numerical version of eqn (4). We plot this in Fig. 5c (red line) and find that this model captures the point of deviation from the 3/2 response (black dotted line), as well as the slope in the super-Hertzian regime. We note that, as we have zoomed in heavily on this section of our data, we can now see that the prediction (blue line) which comes from our nondimensionalization (eqn (4)) is off by a factor of order 1 ($\approx$1.4). Indeed, if the same zoom is performed for all particle types in Fig. 4 we find similar kinds of deviations, where the true stiffness of the columns is off from our prediction by a factor of $\pm$2. We expect that this comes from the approximations that we made in arriving at eqn (3), as well as second-order corrections coming from the exact shape of the grains, their frictional properties, the mode of construction of the column, *etc.*

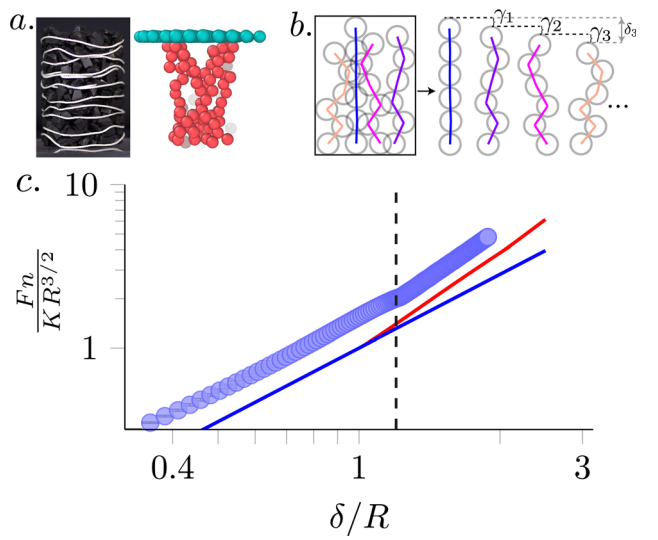

Fig. 5 (a) In our simulations, we find that as we compress a column made up of particles whose material properties are modeled after the chopped rubber, the number of force chains increases. (b) An illustration of our mathematical model. As the column gets loaded, subsequent force chains become active, supporting the load in parallel and increasing the stiffness of the column. The necessary displacement to activate force chain i (δ_i) is shown for i = 3, and the displacement between subsequent force chains forming γ_i is shown for i = 1, 2, 3. (c) If we zoom in on the high-load portion of the force–displacement curve for the rubber chunks and overlay the numerical result of our mathematical model (eqn (4), red line) we find that our predictions capture the deviation from classical Hertzian behavior (blue line) of the columns, as well as the slope in the super-Hertzian regime.

In Fig. 4b, we find that the columns exhibit a similar response regardless of the amount of external fiber that they are constructed with. We show this again in Fig. 6b, where we plot the average total stiffness of each column K_t normalized by the stiffness of a column constructed with the lowest possible ψ_e, and $\psi_i = 0$ against ψ_e and ψ_i. We find that increasing ψ_e increases the stiffness of some columns by at most a factor of $\approx$1.8 (however this finding is not universal to all particle types) and increasing ψ_i has no regular effect on the column stiffness. In other words, the fiber effect on the columns is mostly kinematic, providing constraints on motion, while the grains set the material response.

We did find, analogous to the work in Guerra (2021),[53] that increasing the amount of fiber, inside or out, increased the stability of the particles in the columns. When loading a column with a low amount of internal and external fiber, we noticed large shifts in grain positions, which resulted in a "jagged" force–displacement response (Fig. 6d inset black). Increasing the amount of fiber led to "smoother" curves (Fig. 6d inset orange). To quantify this effect, we sum the

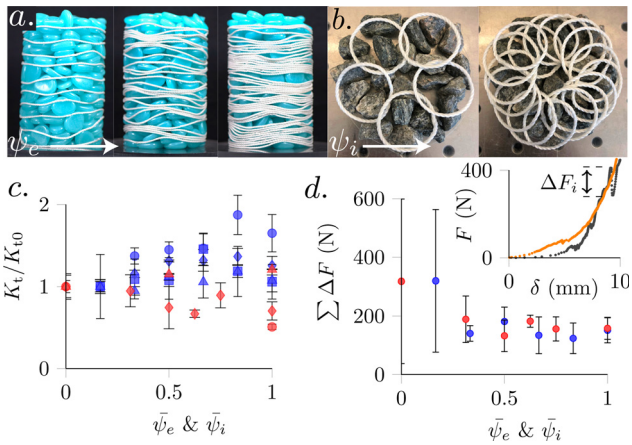

Fig. 6 Columns with increasing (a) ψ_e and (b) ψ_i from left to right. (c) The stiffness of a column K_t normalized by the stiffness of a column at the minimum ψ_e and ψ_i *vs.* $\bar{\psi}_e$ (blue) and $\bar{\psi}_i$ (red) where the bar indicates that the value of ψ is normalized by the maximum value that we used in our experiments, where $\psi_{e\,max}$ = 0.64 and $\psi_{i\,max}$ = 0.05. We find that the addition of fiber, inside or out, has a small and irregular (*i.e.* grain-type-dependant) effect on the stiffness of a column as compared to the grain stiffness. (d) We plot the sum of the height of jumps in the force against the amount of fiber, and find that both interior and exterior fiber increases the smoothness of the loading response. An example is shown in the inset, where the black curve has no internal and little external fiber, and the orange curve has the same amount of external fiber, and ψ_i = 0.05.

difference between all adjacent peaks and troughs throughout the force–displacement profile, which we call $\sum\Delta F$. We plot this value in Fig. 6d and indeed find that it decreases with both ψ_e and ψ_i. Experiments also suggest that internal loops increase the maximum load bearing capacity of the column, by preventing rocks from being crushed under the compressive loads. Preliminary results indicate that columns can withstand higher ultimate loads, but fail in an explosive manner as the bounding loops fracture, allowing particles to be forcibly ejected from the column. A mechanistic understanding of the ultimate load of elastogranular columns is beyond the scope of this work.

3 Beams

The elastogranular columns characterized in the preceding section are formed by a layer-by-layer assembly which includes elements (loops of fiber) that act to prevent grains from escaping laterally, and ensure that the column will remain stable under large compressive loads. However, since the columns lack elastic elements that resist deformation in the long axis of the column, the structures are remarkably weak in shear. By maintaining a residual compressive load, or prestress, the structures can resist shearing and bending, and self-support their weight (Fig. 7). In the following section, we will form cantilevered beams and characterize their effective shear modulus. Since the beams are not homogenous or isotropic, classical relations between E, G, and ν do not hold. While Euler–Bernoulli beam theory represents the simplest model for a cantilever beam, since these structures are shearable, we will develop insight into their shear modulus by employing the Timoshenko beam theory.[65]

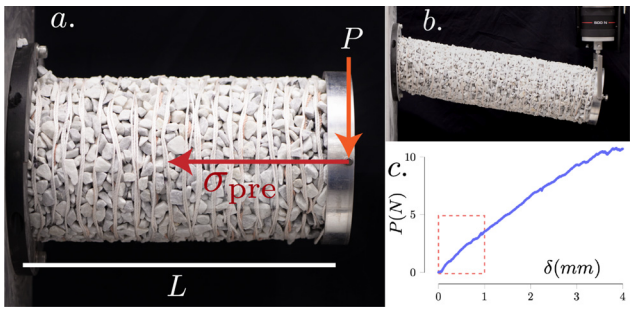

Fig. 7 (a) We clamp columns of length L = 0.24 m and rotate them 90° to form a beam. (b) A picture of the longest stable beam that we constructed. (c) We consider only the first 1 mm of deflection of the beams in our analysis.

3.1 Experiments

To construct beams, we first construct a hollow elastogranular cylinder (with marble, slate, and plastic particles) using a similar process as outlined for the columns above (interior loops of radius 15 mm, exterior loops of radius 60 mm), with removable mylar film along the inner and outer diameter. Through the middle of each cylinder we run a flexible wire rope (Extra-Flexible Wire Rope 3/16″), with one end attached to a solid aluminum cap at the top of the cylinder which acts to clamp down the structure with a force which we refer to as the "pre-compression" (F_{pre}). We include this pre-compression so that the beam does not collapse when we eventually rotate it. The other end is attached to a DDE-500N-002-000 miniature in-line load cell, allowing us to measure (F_{pre}), which we vary by adjusting the length of the flexible wire. We then rotate the set-up 90°, and apply a cyclical load perpendicular to the normal axis of the beam. Displacement (δ) within the force–displacement curves represents the distance that the end-point of the beam is deflected. All applied beam theory is valid only for small deflections and so we limit our analysis to the initial 1 mm of deflection (Fig. 7c). To further ensure this validity, one would naturally choose beam lengths that are lower than the elastogravity length, which is found through a balance of the force required for beam deflection and the force due to gravity. However, we don't know the expected beam deflection *a priori*, so instead we select a length L = 240 mm, which we found, for all our particle types, ensures that $\delta_g/D \ll 1$ ($\delta_g/D < 0.1$) where δ_g is the deflection due to gravity (which arises when we orient the beam horizontally), and D is the diameter of the beam (for instance, we would not include results from the beams shown in Fig. 1b and 7b, we include these simply to show how robust the beams are to large deflections). To mitigate the end-shortening caused by our imposed deflection, we set the beam on a roller support (RB Linear Air Bearing Slide model A109 with 300 mm travel).

3.2 Analysis

As we deflect these beams, there is significant shearing between adjacent grains. We can understand the expected deflection of

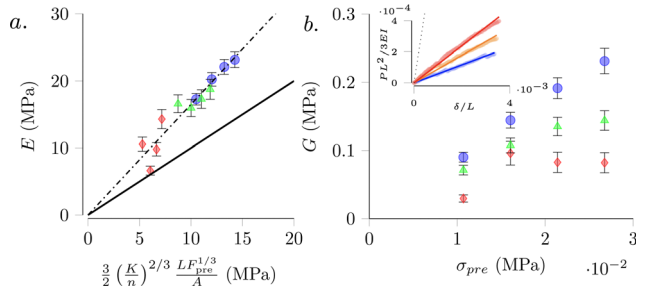

Fig. 8 (a) A plot of the fit Young's moduli at different values of pre-stress from experiments compared to our expected value based on eqn (6) (green – slate, red – plastic, blue – marble). The solid line is our prediction, and the dotted line shows that indeed the data collapse and seem to scale as we expect, but our prediction is off by a constant factor. (b) In the inset, we show linear fits (solid lines) to the force which is required to deflect slate beams at different pre-compressions (increasing blue → yellow → red). We find that these are around an order of magnitude smaller than the Euler–Bernoulli prediction (gray dotted line). Using eqn (5), we can employ these fitted values to find a value of the shear modulus, which we plot against the pre-stress ($\sigma_{pre} = F_{pre}/A$) on a column in the main frame.

beams with shear using Timoshenko–Ehrenfest Beam theory,[65] which predicts the following deflection per unit force:

$$\frac{\delta}{L} = \frac{PL^2}{I}\left(\frac{1}{3E} + \frac{I}{AGkL^2}\right) \quad (5)$$

where P is the load, E is the Young's modulus, L is the length, I is the second moment of area, A is the cross-sectional area, G is the shear modulus, and k is the geometry-dependent Timoshenko shear coefficient of the beam (we used a circular cross-sectional value of 0.89). Note that the first term in the parentheses gives the deflection of a beam with no shear ($G \to \infty$), as given by classical Euler–Bernoulli beam theory,[65] whereas the second term gives the additional deflection which comes from shearing within the beam. In this equation there are two unknown material constants – E and G. We might expect that both depend on F_{pre}. For instance, as the pressure on a granular array increases, so does its shear modulus, as more grains will become more tightly packed and locked in place.[66] Similarly, we would expect E to increase with the pre-compression on the beams because of our above analysis. In the previous section we found that the elastogranular beams have a Hertzian ($F \sim \delta^{3/2}$) response in compression. The Young's modulus is the slope of a linear fit to the force–displacement curve and therefore, since the force–displacement curve is nonlinear, it will change as the beam is compressed. We can find the E by taking the derivative of our relation from the previous analysis

$$E = \frac{L}{A}\frac{\mathrm{d}F}{\mathrm{d}\delta} = \frac{3}{2}\left(\frac{K}{n}\right)^{2/3}\frac{LF_{pre}{}^{1/3}}{A} \quad (6)$$

where we have inserted our earlier estimate (eqn (3)) for the expected stiffness of a column. To test this prediction, we pre-tensioned each elastogranular beam to an initial load in increments of 50 N, from 100 N to 250 N, and then apply a uniaxial cyclical compression test as outlined in the previous section. We synced the internal load cell data and Instron load cell data to find the total load on each cylinder throughout the testing process. We plot fit values of E to these curves against our expected value from eqn (6) in Fig. 8a, and find that the data indeed collapse according to the relation, however, we seem to be off by a constant factor of order 1 ($\approx$1.65) (Fig. 8a, dotted line). Similar to in the previous section, we expect that this comes from the approximations in our model. Because of this constant factor, in the following analysis we will use the values of E found from experiments rather than the result of eqn (6).

We can approximate G by fitting the Timoshenko–Ehrenfest equation to the beam deflection data using a linear regression. We show the results of some regressions in the inset of Fig. 8b, and plot G as a function of pre-compression in Fig. 8b. As expected, as the pre-compression is increased, there is a greater resistance to shear between particles and the extracted shear modulus terms increase accordingly.

4 Conclusions

When sufficiently combined,[10–12,47,53] fiber and grains can form load-bearing columns and beams. The mechanical response of the elastogranular structures that emerge is hierarchical: (i) at very small displacements ($\delta/R \ll 1$), deformation is resisted by friction as the grains rearrange (empirically, $F \sim \delta$); (ii) at small displacements ($\delta/R < 1$), the elastogranular matrix jams, a single force chain propagates the length of the column, and the elastogranular column exhibits a Hertzian force–displacement response ($F \sim \delta^{3/2}$); and finally (iii) at moderate displacements ($\delta/R \approx 1$), multiple force chains sequentially engage at consistent intervals of $\gamma_i = R$, and a "super Hertzian" mechanical response is observed. If there is a new scaling, it appears to be at least ($F \sim \delta^2$), however, this potentially new power law is only observed just above ($\delta/R \approx 1$), and so it would be presumptuous to assume this scaling will hold over a larger range of data, or even that the data will be represented by new power law at all. Our model suggests a mechanism for this stiffening that would continue to increase as additional force chains are formed, indicating that, unless there are other mechanisms at play, the super-Hertzian behavior of these elastogranular columns will not be characterized by a simple power-law.

Fiber both stabilizes the column, and ensures a smooth force–displacement response – neither interior nor exterior loops appear to increase the stiffness of the columns by more than a factor of 2 once there is enough fiber to stabilize the grains. As assembled in this work, there is little to resist shear. However, maintaining a uniaxial compressive prestress on the structures causes them to remain jammed and withstand marginal amounts of shear ($G/E \approx 0.1$). These preloaded columns can form beams: spanning structures capable of bearing transverse loads. The capacity to withstand compression and shear will enable the formation of more complex structures, such as arches (Fig. 1c).

The ability to create rapid, reusable infrastructure components through granular jamming, from inexpensive, commonplace materials, such as rocks and string, presents a new approach to building engineering structures. Elastogranular structures may aid in the construction of temporary shelters during disaster relief efforts, and may enable inexpensive, recyclable, and sustainable architectural elements, all of which can dynamically adapt, unlike traditionally static architecture, in response to a changing climate and environment. Novel fabrication techniques, such as mixing elastic and granular materials (thereby forming an elastogranular matrix) until entanglement causes jamming, utilizing tensegrity mechanisms, or incorporating active matter (*e.g.* targeted root growth) and smart materials (*e.g.* load sensing grains; shape-shifting fibers), will enable the fabrication of structures that are built from local and sustainable materials, and are transformable and adaptable in real-time.

Author contributions

Arman Guerra: mathematical modeling, simulation design, and writing/editing. Casey Lautzenhiser: experimental design, experimentation, and original draft preparation. Xin Jiang: experimental design and initial modeling. Kate Flanagan: experimentation. David Rak: experimentation. Skylar Tibbits: conceptual design. Douglas P. Holmes: Supervision, conceptual design, and writing/editing.

Conflicts of interest

There are no conflicts to declare.

Acknowledgements

The authors gratefully acknowledge the financial support from DARPA (#HR00111810004), and from NSF CMMI-CAREER through Mechanics of Materials and Structures (#1454153). We also thank Mohamad Eydani Asl for initial discussions and preliminary experimental design.

References

1 UNESCO, *Art of dry stone walling, knowledge and techniques*, https://ich.unesco.org/en/RL/art-of-dry-stone-walling-knowledge-and-techniques-01393, 2018, (Accessed on 03/13/2019).
2 A. J. Liu and S. R. Nagel, *Nature*, 1998, **396**, 21–22.
3 T. Majmudar, M. Sperl, S. Luding and R. P. Behringer, *Phys. Rev. Lett.*, 2007, **98**, 058001.
4 C. Song, P. Wang and H. A. Makse, *Nature*, 2008, **453**, 629–632.
5 M. Van Hecke, *J. Phys.: Condens. Matter*, 2009, **22**, 033101.
6 M. Wyart, L. E. Silbert, S. R. Nagel and T. A. Witten, *Phys. Rev. E: Stat., Nonlinear, Soft Matter Phys.*, 2005, **72**, 051306.
7 W. G. Ellenbroek, M. Van Hecke and W. Van Saarloos, *Phys. Rev. E: Stat., Nonlinear, Soft Matter Phys.*, 2009, **80**, 061307.
8 M. Cates, J. Wittmer, J.-P. Bouchaud and P. Claudin, *Phys. Rev. Lett.*, 1998, **81**, 1841.
9 H. M. B. Al-Hashemi and O. S. B. Al-Amoudi, *Powder Technol.*, 2018, **330**, 397–417.
10 P. Aejmelaeus-Lindström, J. Willmann, S. Tibbits, F. Gramazio and M. Kohler, *Granular Matter*, 2016, **18**, 28.
11 K. A. Murphy, N. Reiser, D. Choksy, C. E. Singer and H. M. Jaeger, *Granular Matter*, 2016, **18**, 26.
12 P. Aejmelaeus-Lindström, A. Mirjan, F. Gramazio, M. Kohler, S. Kernizan, B. Sparrman, J. Laucks and S. Tibbits, *Archit. Des.*, 2017, **87**, 82–87.
13 D. Dumont, M. Houze, P. Rambach, T. Salez, S. Patinet and P. Damman, *Phys. Rev. Lett.*, 2018, **120**, 088001.
14 C. McDowell, *Highw. Res. Board, Bull.*, 1959, **231**, 60–66.
15 F. Bell, *Eng. Geol.*, 1996, **42**, 223–237.
16 H. Binici, O. Aksogan and T. Shah, *Constr. Build. Mater.*, 2005, **19**, 313–318.
17 H. Vidal, *Highway research record*, 1969.
18 C. B. Brown and M. S. Sheu, *J. Soil Mech. Found. Div.*, 1975, **101**, 147–165.
19 L. Waldron, *Soil Sci. Soc. Am. J.*, 1977, **41**, 843–849.
20 T. H. Wu, R. M. McOmber, R. T. Erb and P. E. Beal, *J. Geotech. Eng.*, 1988, **114**, 1351–1375.
21 T. H. Wu, P. E. Beal and C. Lan, *J. Geotech. Eng.*, 1988, **114**, 1376–1394.
22 E. Leflaive, Proceedings of the 11th International Conference on Soil Mechanics and Foundation Engineering, San Francisco, USA, 1985, pp. 1787–1790.
23 T. O. Al-Refeai, *Geotextiles Geomembr.*, 1991, **10**, 319–333.
24 R. L. Michalowski and A. Zhao, *J. Geotech. Eng.*, 1996, **122**, 226–234.
25 S. M. Hejazi, M. Sheikhzadeh, S. M. Abtahi and A. Zadhoush, *Constr. Build. Mater.*, 2012, **30**, 100–116.
26 M. H. Maher and D. H. Gray, *J. Geotech. Eng.*, 1990, **116**, 1661–1677.
27 A. Diambra, E. Ibraim, D. M. Wood and A. Russell, *Geotextiles Geomembr.*, 2010, **28**, 238–250.
28 S. M. Tafreshi and A. Dawson, *Geotextiles Geomembr.*, 2012, **32**, 55–68.
29 A. Diambra and E. Ibraim, *Géotechnique*, 2015, **65**, 296–308.
30 C.-S. Wu and Y.-S. Hong, *Geotextiles Geomembr.*, 2008, **26**, 302–316.
31 H. Niroumand, K. A. Kassim and C. S. Yah, *Electron. J. Geotech. Eng.*, 2011, **16**, 1477–1499.
32 J. Murray, J. Frost and Y. Wang, *Transp. Res. Rec.*, 2000, **1714**, 9–17.
33 S. R. Kaniraj and V. Gayathri, *Geotextiles Geomembr.*, 2003, **21**, 123–149.
34 S. Ashwin, M. Z. Yamchi and R. K. Bowles, *Phys. Rev. Lett.*, 2013, **110**, 145701.
35 M. Godfrey and M. Moore, *Phys. Rev. Lett.*, 2018, **121**, 075503.
36 H. Ikeda, *Phys. Rev. Lett.*, 2020, **125**, 038001.
37 A. R. Mojdehi, B. Tavakol, W. Royston, D. A. Dillard and D. P. Holmes, *Extreme Mech. Lett.*, 2016, **9**, 237–244.

38 D. J. Schunter Jr, M. Brandenbourger, S. Perriseau and D. P. Holmes, *Phys. Rev. Lett.*, 2018, **120**, 078002.
39 N. Algarra, P. G. Karagiannopoulos, A. Lazarus, D. Vandembroucq and E. Kolb, *Phys. Rev. E*, 2018, **97**, 022901.
40 D. J. Schunter, M. Boucher and D. P. Holmes, *Granular Matter*, 2020, **22**, 1–6.
41 D. Schunter Jr, R. Czech and D. P. Holmes, *Soft Matter*, 2020, **16**, 2039–2044.
42 A. G. Athanassiadis, M. Z. Miskin, P. Kaplan, N. Rodenberg, S. H. Lee, J. Merritt, E. Brown, J. Amend, H. Lipson and H. M. Jaeger, *Soft Matter*, 2014, **10**, 48–59.
43 E. Azéma, F. Radjai and F. Dubois, *Phys. Rev. E: Stat., Nonlinear, Soft Matter Phys.*, 2013, **87**, 062203.
44 M. Fauconneau, F. K. Wittel and H. J. Herrmann, *Granular Matter*, 2016, **18**, 27.
45 Y. Liu, X. Zhou, Z. You, S. Yao, F. Gong and H. Wang, *Constr. Build. Mater.*, 2017, **143**, 169–178.
46 P. S. Iliev, F. K. Wittel and H. J. Herrmann, *Comput. Part. Mech.*, 2018, **5**, 507–516.
47 Z. Cohen, N. Elberfeld, A. Moorman, J. Laucks, S. Kernizan, D. P. Holmes and S. Tibbits, *Technol./Archit. + Des.*, 2020, **4**(2), 211–220.
48 A. M. Thompson, A. C. Paul and N. J. Balster, *Trans. ASABE*, 2008, **51**, 499–514.
49 C. Clanton, D. R. Schmidt, R. E. Nicolai, L. D. Jacobson, P. R. Goodrich, K. A. Janni and J. R. Bicudo, *Appl. Eng. Agric.*, 2001, **17**, 849.
50 C.-S. Wu, Y.-S. Hong and H.-C. Lin, *Comput. Geotech.*, 2009, **36**, 226–240.
51 C.-S. Wu and Y.-S. Hong, *Geotextiles Geomembr.*, 2014, **42**, 339–347.
52 Y.-S. Hong, C.-S. Wu, C.-M. Kou and C.-H. Chang, *Geotextiles Geomembr.*, 2017, **45**, 391–405.
53 A. Guerra and D. P. Holmes, *Soft Matter*, 2021, **17**, 7662–7669.
54 S. Plimpton, *J. Comput. Phys.*, 1995, **117**, 1–19.
55 A. Stukowski, *Modell. Simul. Mater. Sci. Eng.*, 2009, **18**, 015012.
56 H. Hertz, *Ueber die Berührung fester elastischer Körper*, De Gruyter, 2021.
57 K. L. Johnson and K. L. Johnson, *Contact mechanics*, Cambridge university press, 1987.
58 A. C. Ugural, *Mechanics of materials*, John Wiley & Sons, 2007.
59 J. H. Snoeijer, T. J. Vlugt, M. van Hecke and W. van Saarloos, *Phys. Rev. Lett.*, 2004, **92**, 054302.
60 J. Peters, M. Muthuswamy, J. Wibowo and A. Tordesillas, *Phys. Rev. E: Stat., Nonlinear, Soft Matter Phys.*, 2005, **72**, 041307.
61 L. Zhang, N. G. H. Nguyen, S. Lambert, F. Nicot, F. Prunier and I. Djeran-Maigre, *Eur. J. Environ. Civil Eng.*, 2017, **21**, 874–895.
62 R. K. Pal, R. B. de Macedo and J. E. Andrade, *Granular Matter*, 2021, **23**, 1–14.
63 B. P. Tighe, J. H. Snoeijer, T. J. Vlugt and M. van Hecke, *Soft Matter*, 2010, **6**, 2908–2917.
64 B. Noble and M. Hussain, *Int. J. Eng. Sci.*, 1969, **7**, 1149–1161.
65 A. P. Boresi, R. J. Schmidt and O. M. Sidebottom*et al.*, *Advanced mechanics of materials*, Wiley, New York, 1985, vol. 6.
66 M. A. Sayeed, K. Suzuki and M. M. Rahman*et al.*, PhD thesis, IJENS Publishers, 2011.

